



CHORUS

This is the accepted manuscript made available via CHORUS. The article has been published as:

Predictive model for convective flows induced by surface reactivity contrast

Scott M. Davidson, Rob G. H. Lammertink, and Ali Mani

Phys. Rev. Fluids **3**, 053701 — Published 17 May 2018

DOI: [10.1103/PhysRevFluids.3.053701](https://doi.org/10.1103/PhysRevFluids.3.053701)

A Predictive Model for Convective Flows Induced by Surface Reactivity Contrast

Scott M. Davidson¹, Rob G.H. Lammertink², and Ali Mani^{*1}

¹Department of Mechanical Engineering, Stanford University, Stanford, CA 94305,
USA

²Soft Matter, Fluidics and Interfaces, Mesa+ Institute for Nanotechnology,
University of Twente, 7500 AE Enschede, The Netherlands

February 15, 2018

Abstract

Concentration gradients in a fluid adjacent to a reactive surface due to contrast in surface reactivity generate convective flows. These flows result from contributions by electro and diffusio osmotic phenomena. In this study we have analyzed reactive patterns that release and consume protons, analogous to bimetallic catalytic conversion of peroxide. Similar systems have typically been studied using either scaling analysis to predict trends or costly numerical simulation. Here, we present a simple analytical model, bridging the gap in quantitative understanding between scaling relations and simulations, to predict the induced potentials and consequent velocities in such systems without the use of any fitting parameters. Our model is tested against direct numerical solutions to the coupled Poisson, Nernst–Planck, and Stokes equations. Predicted slip velocities from the model and simulations agree to within a factor of ≈ 2 over a multiple order-of-magnitude change in the input parameters. Our analysis can be used to predict enhancement of mass transport and the resulting impact on overall catalytic conversion, and is also applicable to predicting the speed of catalytic nanomotors.

*Corresponding author: alimani@stanford.edu

1 Introduction

The ability of catalytic micropumps to generate motion from chemical energy has opened many possibilities [1–3]. By generating convection at the microscale, catalytic micropumps can enhance transport rates to surfaces where diffusion would otherwise be limiting [4]. Due to their use of local chemical energy, catalytic micropumps don't suffer from some of the issues associated with other methods of generating flow at the microscale. Pressure-driven flow is inefficient due to the rapid increase in hydraulic resistance with decreasing length scale. Meanwhile other electrokinetic methods such as conventional electroosmotic flow and induced-charge electroosmosis [5, 6] require imposition of external electric fields or, in the case of alternating-current electroosmosis, electrical connection of micro-electrodes [7–9].

A number of studies, which we review below, have contributed to identification of mechanisms leading to electrostatic potential gradients and fluid flow in systems involving surface reactivity contrasts. However, a quantitative understanding that would directly connect the outcome of induced potentials and flow fields to the key input parameters is yet to be developed. Typically, numerical simulation has been used to make quantitative connections, but numerical simulation is a costly approach in terms of computational time and resources. Ideally, it would be desirable to have an algebraic model predicting this outcome. As we shall see, flow fields in these systems can have a nonmonotonic dependence on input and therefore it is crucial to have a model that goes beyond simple scaling relations in large and small parameter limits. Our study presents such models for a canonical problem, directly relating input parameters to quantities of interest without using any tuning parameters.

The literature relevant to understanding of catalytic micropumps can be placed into several categories each of which we expand on below. First, micropumps where surface reactions induce electric fields which generate electroosmotic flow, the primary focus of this work. Second, micropumps based on diffusioosmotic mechanisms. Finally, when the reactions occur on a particle, then the same physical mechanisms will lead to self-phoretic behavior instead of pumping.

Surfaces with nonuniform catalytic reactivity generate flow by multiple mechanisms [10]. One mechanism, electroosmosis, refers to flows generated when reaction-induced electric fields, driving current through the fluid, act on surface electric double layers screening the surface charge. This mechanism has been studied using a silver disc plated on a gold substrate immersed in a hydrogen peroxide solution [1, 11] as well as for interdigitated gold and platinum electrodes [12]. Ibele *et al.* showed that different fuels can generate flow by the same mechanism by developing a system using hydrazine fuels [13]. Farniya and coworkers developed a technique for inferring chemical reaction rates and ion impurities in electrocatalytic micropumps by fitting simulations to detailed experiments measuring proton concentrations with fluorescence microscopy and tracking of particles with positive and negative surface charges to measure flow velocities and electric fields [14]. In other experiments it has been shown that separating the electrodes on opposite sides of a membrane [15] and utilizing the high surface charge of doped silicon provide promising avenues for enhancing the flow rates

generated by electrocatalytic micropumps [16]. Recent simulations by Esplandiu *et al.* analyzed important parameters in self-electroosmotic pumps and suggested that the induced electric fields are dependent on ionic strength, not total conductivity [17]. However their model assumed that only protons contribute to the net current and ignored bulk equilibrium reactions.

A second mechanism, diffusioosmosis, refers to flows generated by the presence of species concentration gradients tangent to the surface. When the concentration gradients are caused by nonuniform reactivity of the surface itself the flows they generate are called self-diffusioosmotic. Such gradients may generate flows in multiple ways depending on whether the solution is an electrolyte [18] or not [19]. In electrolyte solutions, gradients of species concentrations generate diffusioosmotic flows due to the dependence of the pressure difference across the Debye screening layer on solution conductivity. The surface pressure is proportional to the local conductivity, so concentration gradients along the surface generate pressure gradients and hence flow. Also, for electrolytes where the positive and negative species have different diffusivities, concentration gradients cause internal electric fields which act on the Debye layer to generate flow. Diffusioosmotic flows have been used to develop microfluidic pumps [3]. Hong *et al.* utilized the photocatalytic sensitivity of titanium-dioxide to generate a diffusioosmotic micropump controllable by light [20]. Niu *et al.* showed that even in micromolar salt concentrations, an ion-exchange resin can be used to create a self-diffusioosmotic micropump [21].

Although we are primarily concerned with electrocatalytic micropumps, much research into electrocatalytic conversion of chemical to mechanical energy has focused on reaction induced propulsion of nano-swimmers i.e. self-electrophoresis and self-diffusiophoresis. The same mechanisms which cause pumping on a fixed surface lead to swimming of a particle with varying surface reactivity. Such self-phoretic mechanisms for motion were originally investigated in the context of cell motion [22, 23]. Early experiments demonstrating reaction-induced propulsion in non-living systems utilized bimetallic particles in peroxide solutions [24–26]. Various proposed mechanisms explaining their motion were proposed, and of these self-electrophoresis was found to be dominant [12, 27]. Velocities on the order $10 \mu\text{m/s}$ were reported. Nanomachines such as these have created much excitement due to their potential to revolutionize fields such as drug delivery and biological sensing [28–31].

A number of theoretical studies have been performed to better understand self-catalytic swimming. Golestanian showed how asymmetric reaction induced concentration gradients result in the propulsion of particles by self-diffusiophoretic mechanisms [32]. Moran and Posner investigated the self-electrophoretic mechanism by performing direct numerical simulations of the bulk transport equations coupled initially to fixed surface fluxes [33] which they refined by considering surface reaction kinetics [34]. They also analyzed the reduction in swimming speed with background electrolyte concentration [35]. However, their model predicted a quadratic relationship between swimming speed and peroxide concentration unlike the linear dependence observed in experiments. Yariv studied the problem using matched asymptotic expansions in the limit of thin electrical double layers and long-slender rods, predicting propulsion in experimentally observed direction [36]. Sabass and Seifert found that in the presence of background salt, the decrease in pH with increased peroxide concentration

can alleviate diffusive limitations on proton transport [37]. Self-consistent nonlocal feedback theory, relating local fluxes to changes in the induced potential field, was developed to further improve understanding of electrocatalytic motors [38] and inspiring our analysis. Further theoretical studies have found that the optimal location for surface reactivity is concentrated at the poles of the swimmer [39], a geometrical effect which may guide design of micropumps, and that bulk peroxide decomposition can significantly affect swimming speeds [40].

Here, we investigate the relation between surface reactivity patterns and the fluid flow they generate. For this, we analyzed the scaling relation of the induced potential (gradient) and velocity with surface reactivity. The system corresponds to a pattern of catalytic sites with distinct reaction rate constants (expressed by their corresponding second Damköhler numbers). We provide physical insight into how the different components of the induced potential lead to a balance of fluxes in the system. We also derive a simple model capturing the induced potential and flow velocity and compare this with direct numerical simulations of the governing transport equations.

2 Model Problem

Many combinations of patterned metals and electrolytes lead to reactions which generate the asymmetric ion concentrations necessary to induce this type of flow [27]. In this work, we focus on electrocatalytic hydrogen peroxide oxidation at Pt next to its reduction on Au surfaces. The oxidation generates electrons and protons, while the reduction consumes protons and electrons. This asymmetric surface reaction pair generates and depletes protons near the surface resulting in a reaction induced charge distribution and electric field. The forces on the fluid caused by the induced electric field acting on the induced charge distribution gives rise to an electroosmotic flow which is driven by the electrocatalytic conversion.

Specifically, we model a two-dimensional domain of width λ and height L consisting of an electrolyte between a reactive surface and a reservoir as shown in Figure (1). The domain is periodic in the tangential x direction, and thus λ represents the period of a repeating patterned surface of which we simulate one period. This surface is modeled as completely flat, with a step change in surface reactivity at the intersection of the Au and Pt surface regions. The background electrolyte contains four species: protons H^+ , hydroxide ions OH^- , hydrogen peroxide H_2O_2 , and molecular oxygen O_2 . Peroxide oxidation at the platinum anode is given by



and reduction at the gold cathode is given by



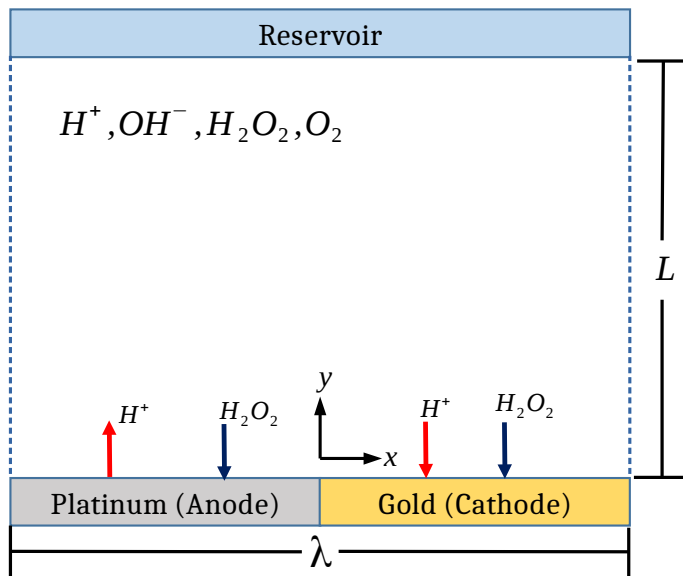


Figure 1: (Color online) Schematic showing the model problem. The electrocatalytic surface reaction pair consists of Gold (Au) and Platinum (Pt) at a periodic width of λ in contact with the electrolyte containing protons, hydroxide ions, hydrogen peroxide and oxygen.

This choice of reaction mechanism governing the decomposition of H_2O_2 has been successfully used in previous studies [17, 33]. However, there remains uncertainty regarding the precise mechanism of peroxide decomposition at platinum and gold surfaces. Mechanisms other than the one used here have been proposed [41, 42]. Our simulations and model could be modified to account for alternative mechanisms.

In this work, we only explicitly simulate the concentrations of the two ionic species, protons and hydroxide ions. We assume that the concentration of peroxide is constant over relevant timescales so its transport can be ignored. This assumption is justified with scaling arguments in Section (2.3). Transport of oxygen can be ignored because in the dilute limit oxygen only affects the system through the anode reactions. However, we assume that the anode reaction only proceeds in the forward direction in which oxygen does not participate [34].

2.1 Governing Equations

This system is governed by the coupled Poisson-Nernst-Planck (PNP) equations for ion transport and unsteady Stokes equations of fluid motion along with appropriate surface and bulk reactions. The PNP equations relate species concentration change to advection, diffusion, reaction, and electromigration fluxes. Transport of ionic species is coupled through the Poisson equation for the electric potential.

In dimensionless form they are given by

$$\frac{\partial c_i}{\partial t} + \nabla \cdot (\mathbf{u}c_i) = D_i \nabla \cdot (\nabla c_i + z_i c_i \nabla \phi) + R_i \quad (3)$$

$$-2\epsilon^2 \nabla^2 \phi = \sum_i z_i c_i \quad (4)$$

where $c_i = \tilde{c}_i/c_0$ is the dimensionless concentration of species i which has valence z_i and diffusivity $D_i = \tilde{D}_i/D_0$, where the $\tilde{}$ represent dimensional quantities when there is a dimensionless counterpart. c_0 and D_0 are arbitrary reference values for concentration and diffusivity. In this study we reference diffusivities to the diffusivity of hydroxide ions $D_0 = 5.273 \times 10^{-9} \text{ m}^2/\text{s}$ [34] and concentrations to the bulk concentrations of H^+ and OH^- in pure water, $c_0 = \sqrt{K_w} = 1 \times 10^{-7} \text{ M}$ where K_w is the water equilibrium constant. $\phi = \tilde{\phi}/V_T$ is the electrostatic potential normalized by the thermal voltage $V_T = RT/F \approx 25 \text{ mV}$ where R is the ideal gas constant, T the temperature, and F the Faraday constant. $\mathbf{u} = \tilde{\mathbf{u}}/(D_0/\lambda)$ is the fluid velocity normalized by the diffusion velocity. $t = t/t_0$ where $t_0 = \lambda^2/D_0$ is the diffusion time. The coefficient ϵ is the dimensionless Debye length $\epsilon = \lambda_D/\lambda$ where for our case of a symmetric binary electrolyte $\lambda_D = \sqrt{\epsilon V_T/2Fc_0}$ where ϵ is the permittivity of water. $R_i = \tilde{R}_i/(c_0/t_0)$ is a bulk reaction term. For hydrogen peroxide and molecular oxygen, $R_i = 0$. For protons and hydroxide ions, $R_i = Da_b (K_w/c_0^2 - c_+ c_-)$ which enforces water self-ionization. $Da_b = k_b \lambda^2 c_0/D_0$ is a dimensionless bulk Damköhler number where k_b is the bulk water recombination reaction rate constant and c_+ and c_- are proton and hydroxide ion concentrations respectively. With this nondimensionalization, all lengths are normalized by λ and thus the dimensionless width is 1. We chose an aspect ratio of $L/\lambda = 4$, which is large enough that the reservoir boundary conditions do not affect the simulated flow near the electrodes.

The Stokes equations for momentum conservation along with continuity which enforces the incompressibility of water are

$$\frac{1}{Sc} \frac{\partial \mathbf{u}}{\partial t} = -\nabla p + \nabla^2 \mathbf{u} - \frac{\kappa}{2\epsilon^2} \rho_e \nabla \phi \quad (5)$$

$$\nabla \cdot \mathbf{u} = 0 \quad (6)$$

Here we have included the electric body force term, and ignored the nonlinear inertial term because it is small relative to the viscous and electric body force terms as verified in Section 3.1. $p = \tilde{p}/(\mu D_0/\lambda^2)$ is the pressure, and $\rho_e = \sum_i z_i c_i/c_0$ the charge density. The Schmidt number $Sc = \mu/\rho D_0$ where μ is the dynamic viscosity and ρ the density of water, and the electrohydrodynamic coupling constant $\kappa = \epsilon V_T^2/\mu D_0$. Note that we do not include any chemiosmotic forces (i.e. forces due to nonionic solute-wall interactions) because gradients in nonionic solutes (O_2 and H_2O_2) are expected to be very small. However, the diffusioosmotic forces due to internal electric fields caused by salt concentration gradients with ions of different diffusivities are naturally included by this formulation.

2.2 Boundary Conditions

The boundary condition for the Stokes equations at both the electrodes ($y = 0$) and reservoir ($y = 4$) is given by

$$\mathbf{u} = \mathbf{0} \quad (7)$$

due to the no-slip and no-penetration conditions at the solid surface along with our assumption of a stationary reservoir.

The potential boundary condition at the electrodes is given by

$$\phi = 0 \quad (8)$$

thus representing the constant electric potential of a conductive metal surface which we have arbitrarily set to zero as a reference. Because we resolve the Debye layer in our simulation domain, the zeta potential does not directly enter this boundary condition. Due to the thinness of the Stern layer to the Debye length for the dilute conditions studied, we omit a Stern layer correction [17, 34]. We have ignored other mechanisms which would induce a zeta potential [43] in order to focus on the reaction-induced potential as has been done previously [34]. Inclusion of a fixed zeta potential at each electrode would be a useful extension of the model. The potential boundary condition at the reservoir is

$$\frac{\partial \phi}{\partial y} = 0 \quad (9)$$

or zero normal electric field. As with the reservoir boundary condition for the momentum equations, this condition is valid for sufficiently large L/λ such that, in the absence of external electric fields, electric fields induced by the reactions decay before the reservoir. In other words, for this boundary condition to be valid, we expect that the potential at the reservoir should be approximately constant. The use of a Neumann boundary condition, instead of Dirichlet, at the reservoir allows the potential difference between the surface and reservoir to adjust as the simulation evolves until it reaches a steady-state at which all fluxes are in balance as described in Section 3.1.

For species transport, anions do not participate in either of the surface reactions, so a no-flux boundary condition is enforced on the entire surface. This reduces to

$$\frac{\partial c_-}{\partial y} - c_- \frac{\partial \phi}{\partial y} = 0 \quad (10)$$

For cations, different boundary conditions are used for the platinum and gold portions of the surface. Both are derived by matching the combined electromigration and diffusion fluxes with the

surface reaction flux. The platinum ($-1/2 < x < 0$) and gold ($0 < x < 1/2$) boundary conditions respectively are

$$-D_+ \left(\frac{\partial c_+}{\partial y} + c_+ \frac{\partial \phi}{\partial y} \right) = D_+ Da_a \quad (11)$$

$$-D_+ \left(\frac{\partial c_+}{\partial y} + c_+ \frac{\partial \phi}{\partial y} \right) = -D_+ Da_c c_+^2 \quad (12)$$

where $Da_a = k_{0,anode} \lambda \tilde{c}_{H_2O_2} / \tilde{D}_+ c_0$ is the anode Damköhler number and $Da_c = k_{r,cathode} \lambda \tilde{c}_{H_2O_2} c_0 / \tilde{D}_+$ is the cathode Damköhler number defining the dimensionless anode and cathode reaction rates. These Damköhler numbers represent ratios of reaction timescales to diffusive transport timescales, and hence by varying them we can consider regimes with different limiting mechanisms where reaction at one electrode versus the other controls the process. Both of these boundary conditions assume that the reactions proceed only in the forward direction and that the Stern layer potential drops are sufficiently small that reaction rate coefficients can be treated as constants.

The reservoir boundary condition for both species is simply a Dirichlet condition at the reservoir concentration

$$c_+ = c_- = 1 \quad (13)$$

The left and right boundary are treated as periodic boundaries.

2.3 Validity Regime of Two-Species Approximation

Our assumption that we can treat the concentration of H_2O_2 as a constant is valid so long as the timescale associated with changes in the concentration of H_2O_2 is much longer than dynamically relevant timescales of the system. To estimate this timescale, we start with the balance of reactive and diffusive fluxes at the anode surface. The scaling of these fluxes can be written in dimensionless form as

$$j_{\text{reac}} \sim \frac{Da_a D_+ c_{H_2O_2}}{c_{H_2O_2,0}} \quad (14)$$

$$j_{\text{diff}} \sim \frac{D_{H_2O_2} \Delta c_{H_2O_2}}{l} \quad (15)$$

where l is a characteristic length scale over which the concentration of H_2O_2 changes by $\Delta c_{H_2O_2}$, and $c_{H_2O_2,0}$ is its initial concentration. As a conservative choice for l , we choose the diffusion length $l \sim \sqrt{D_{H_2O_2} t}$. This choice is conservative because additional mixing from the induced flow would only

shorten the length scale. Substituting this value for l into (15), equating the two fluxes, and solving for t gives a scaling for the time associated with a given change in H_2O_2 concentration

$$t_{\text{H}_2\text{O}_2} \sim \left(\frac{\Delta c_{\text{H}_2\text{O}_2}}{c_{\text{H}_2\text{O}_2}} \right)^2 \frac{D_{\text{H}_2\text{O}_2} c_{\text{H}_2\text{O}_2,0}^2}{Da_a^2 D_+^2} \quad (16)$$

In the cases investigated in this study, over dynamically relevant times, which will be at worst $t \sim 1$ (the diffusion time across the domain), $\Delta c_{\text{H}_2\text{O}_2}/c_{\text{H}_2\text{O}_2}$ is small. Therefore, in effectively unbounded domains such as the current study, it is justifiable to ignore changes in H_2O_2 concentration over intermediate timescales which are long relative to system dynamics but short relative to timescales for depletion of H_2O_2 at the surface. For longer term behavior, one may adopt our solution as a quasi-steady solution in which the bulk concentration of H_2O_2 is adjusted gradually with time. In this case (16) would imply that the length scale of depletion of H_2O_2 would be much longer than λ while varying slowly in time. Another possibility is the presence of an effective reservoir H_2O_2 concentration, due to either bulk mixing or for nano-motors the motion of the swimmer itself, in which case a suitable H_2O_2 concentration may be assumed.

2.4 Computational Framework

We solve the governing equations using a custom written OpenMP parallel c++ code described thoroughly and compared against a commercial solver in [44]. The code uses second order staggered finite differences to discretize the governing equations where species concentrations, electric potential and pressure fields are stored at cell centers while velocities and fluxes are stored at cell faces. The linear Poisson and Poisson-like equations for pressure, electric potential, and momentum are solved using a pseudo-spectral method where fourier transforms are performed in the tangential x direction and leaving a tridiagonal system to be solved at each wavenumber in the electrode-normal. Time integration is done with a semi-implicit method which iteratively solves the transport, momentum, and potential equations in a decoupled manner until the full implicit solution for the next timestep is reached. The species transport equations are solved implicitly during each iteration only in the stiff electrode-normal direction. Verification of the accuracy and convergence of the code was performed using the method of manufactured solutions [45]. This code and its variants have been successfully used in previous studies for prediction of chaotic electroconvection [46, 47], induced-charge electro-osmosis [48], and flow over patterned membranes [49]. Mesh convergence testing was performed to ensure that a sufficiently fine mesh was used to resolve the results shown.

3 Results and Analysis

A number of dimensionless parameters are present in the above equations. We summarize these along with the values used in our simulations in table 1. In this work, most of the parameters are held constant while two parameters, the surface Damköhler numbers are varied. For reference to a physical system, the value $\epsilon = 4 \times 10^{-3}$ is representative of a .25mm pattern length λ and pure water reservoir concentration of $c_0 = 1 \times 10^{-7}$ M. Qualitative steady-state fields of concentration, charge density, electric potential and electric field lines, and velocity magnitude with flow streamlines for nominal Damköhler numbers of $Da_a = 1.48$ and $Da_c = 2.68$ are shown in figure 2. These Damköhler numbers come from rate constants $k_{o,anode} = 5.5 \times 10^{-9}$ m/s and $k_{r,cathode} = 1 \text{ m}^7\text{s}^{-1}\text{mol}^{-2}$ [34] and peroxide concentration $c_{\text{H}_2\text{O}_2} = 1 \times 10^{-3}$ M.

Parameter	Description	Formula	Value(s)
ϵ	dimensionless Debye length	λ_D/λ	4×10^{-3}
Sc	Schmidt number	$\mu/\rho D_0$	1000
κ	Electrohydrodynamic coupling constant	$\epsilon V_T^2/\mu D_0$.094
	domain aspect ratio	L/λ	4
D_+	H^+ diffusivity	\tilde{D}_+/D_0	1.7658
D_-	OH^- diffusivity	\tilde{D}_-/D_0	1
Da_b	bulk Damköhler number	$k_b \lambda^2 c_0 / D_0$	9.38×10^4
Da_a	anode Damköhler number	$k_{o,anode} \lambda c_{\text{H}_2\text{O}_2} / D_+ c_0$	$2.5 \times 10^{-3} - 2.5 \times 10^2$
Da_c	cathode Damköhler number	$k_{r,cathode} \lambda c_0 c_{\text{H}_2\text{O}_2} / D_+$	$2.5 \times 10^{-3} - 2.5 \times 10^2$

Table 1: Dimensionless governing parameters

Evident from the concentration field in figure 2a is that, outside of the double layer, the concentration of H^+ , and also OH^- from electroneutrality, is equal to c_0 . The combination of water equilibrium and electroneutrality prevent concentration gradients from forming in the bulk. This would change if other ionic species were present. Note the expanded y scale in figure 2a and b.

The charge density field along with electric field lines are shown in figure 2b. Notable from the electric field lines are a small region near the anode around $y = .002$ and a larger region above the cathode around $y = .018$ where field lines intersect. These correspond to regions where bulk charge is present causing the electric field to not be divergence free. However, the charge at these locations is too small to be seen because we have chosen the color scale based on the largest charge density magnitude in the domain. Similar features have been observed previously [34]. These locations where field lines converge result from a superposition of field lines in the bulk which point from the anode to the cathode transporting the current and field lines associated with the double layer whose direction is determined by the local zeta potential. When these types of field lines point in opposite directions,

then there can be a location at which the direction of the overall electric field switches and hence field lines intersect. In this case, the zeta potential is positive over most of the surface with field lines pointing away from the surface and necessitating the change in direction above the cathode. However, there is a small region near the center of the anode where the zeta potential switches sign leading to field lines near the surface pointing toward the anode which must change direction.

The electric field lines in the bulk can be seen more clearly in figure 2c along with the associated electric potential. These electric field lines act on the charged Debye layer to generate the flow field shown in figure 2d consisting of a pair of counter-rotating vortices.

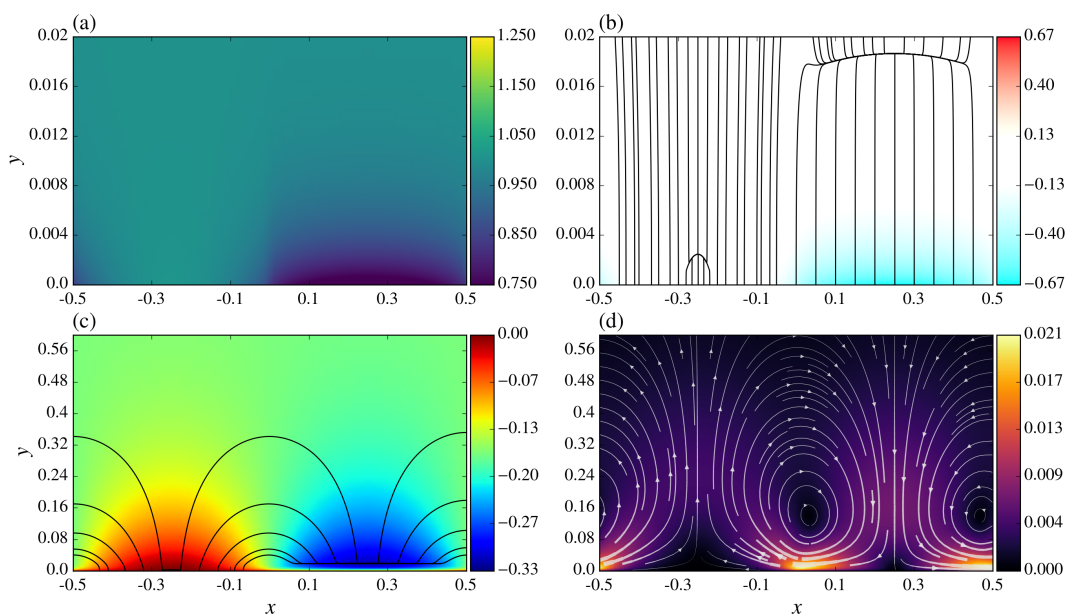


Figure 2: (Color online) Field quantities for $Da_a = 1.48$, $Da_c = 2.68$. (a) H^+ concentration field. (b) ρ_e field with electric field lines. (c) ϕ field with electric field lines. (d) velocity magnitude field with streamlines.

One quantity of interest is the induced potential and particularly the induced potential difference between the surface and far field which we label ϕ_∞ . Figure 3 shows induced electric potential and associated electric field lines for different values of the anode Damköhler number. The color scales in the plots have been set to emphasize variations about ϕ_∞ for each case and do not necessarily contain the zero potential of the surface. One consequence of this choice is the potential field within the double layer saturates in 3a and 3c leading to a sharp change in the color. As the ratio of Damköhler numbers changes, the sign of the induced net electric potential changes, and two patterns in the potential field are evident. First there is a 1D component associated with the net induced potential drop strongly

visible within the double layer very near the surface and varying only in the y direction. There is also evident a component of the potential associated with the outer nearly semi-circular electric field lines which doesn't appear to be significantly affected by the changes in Da_a . The superposition of these two components determines the local zeta potential.

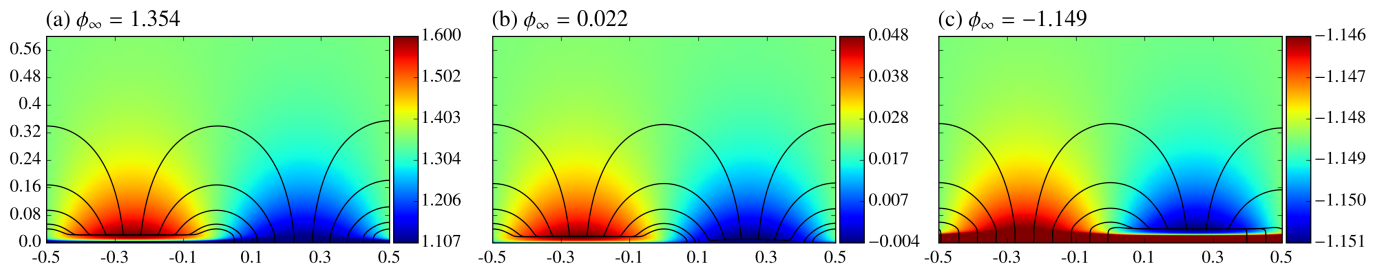


Figure 3: (Color online) Electrostatic potential fields with electric field lines plotted for several values of the Damköhler numbers. (a) $Da_a = 2.5$, $Da_c = .25$ (b) $Da_a = .25$, $Da_c = .25$ (c) $Da_a = .025$, $Da_c = .25$

3.1 An Approximate Model

In this section we develop an approximate model, shown schematically in figure 4, to understand the results of our numerical simulations. Our model utilizes balances of fluxes along with the approximation that current travels along semi-circular electric field lines outside of the double layer. We also take inspiration from asymptotic modeling, e.g. [9, 50], in which an “inner” solution within the thin charged double layer is matched with an “outer” solution valid in the electroneutral bulk. This means that our model requires $\epsilon \ll 1$. We calculate several important quantities which we compare against the results of our numerical simulations. One quantity is the induced potential difference between the surface and bulk $\phi_\infty = \phi(y \rightarrow \infty)$. A second is the reaction-induced zeta potential $\zeta(x) = -(\phi_\infty + \phi_{\text{tan}}(x))$ where $\phi_{\text{tan}}(x)$ describes the variation along the electrode surface just outside of the double layer, analogous to the matching location between asymptotic inner and outer solutions, of the electric potential and hence the tangential electric field responsible for inducing a slip velocity is $E_{\text{tan}} = \frac{d\zeta}{dx} = -\frac{d\phi_{\text{tan}}}{dx}$. These allow us to use the Helmholtz-Smoluchowski equation to calculate a third quantity, the slip velocity u_{slip} .

We start with a balance which helps explain the behavior of ϕ_∞ . At steady state, the total reactive currents at the anode and cathode must balance. At the anode, the reaction rate in our model is determined solely by the constant concentration of H_2O_2 . This means that the system must adjust the reaction rate at the cathode to conserve current. The only way that this adjustment can occur is by changing the surface H^+ concentration to an appropriate average value via an induced potential

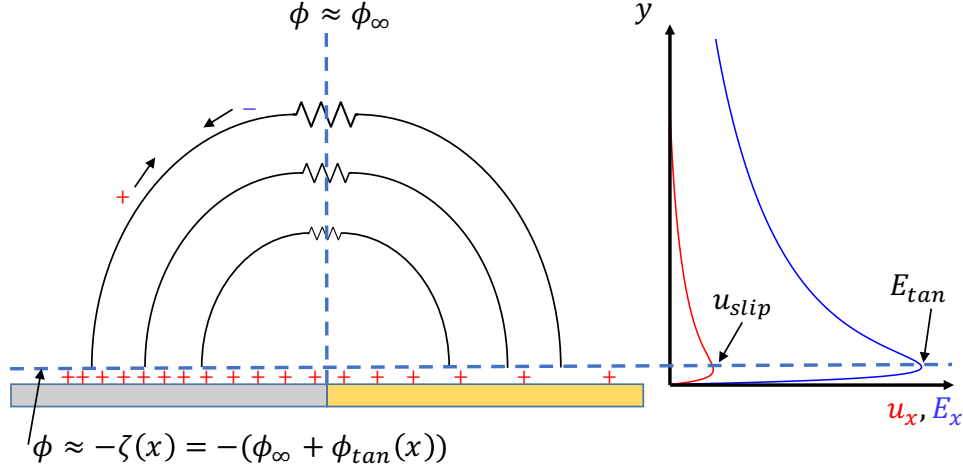


Figure 4: (Color online) Schematic showing conceptually our approximate model, and how we evaluate it against the numerical simulations. The zeta potential just outside the double layer here shown as positively charged. $\zeta(x)$ is calculated as a sum of two terms, the far-field potential ϕ_∞ and a component which varies along the surface $\phi_{tan}(x)$. Current in the bulk travels along semi-circular lines which act as resistors. The model-predicted slip velocity u_{slip} and tangential electric field E_{tan} are compared against the maximum x velocity and x electric field along the line $x = 0$.

ϕ_∞ . We label this estimate of the induced potential $\phi_{\infty,0}$ because we will later calculate ϕ_∞ in a more complete way accounting for transport between anode and cathode, and $\phi_{\infty,0}$ will show up as the first term in that equation. For now, however, we will consider only the ability of a spatially uniform induced zeta potential to lead to a balance of anode and cathode reaction rates. When c_+ obeys a Boltzmann distribution within the double layer, valid for small currents, and is equal to the reservoir concentration outside of the double layer then

$$j_{Pt}^+ = D_+ Da_a \quad (17)$$

$$j_{Au}^+ = (e^{\phi_{\infty,0}})^2 D_+ Da_c \quad (18)$$

where j_i^+ is the magnitude of the local reactive surface flux. Because we have (temporarily) assumed a spatially uniform induced potential and the anode and cathode are of equal size, integrating the reactive flux over each surface amounts to setting these fluxes equal. Doing this and solving for $\phi_{\infty,0}$ gives

$$\phi_{\infty,0} = 1/2 \ln(Da_a/Da_c) \quad (19)$$

Physically, the dependence of $\phi_{\infty,0}$ on the ratio of Damköhler numbers can be interpreted as the potential adjusting to either increase or decrease the surface concentration of H^+ in such a way as to

balance the reaction rates at the electrodes. This leads to a dependence on the ratio of reaction rate constants and the bulk H^+ concentration, but not on the H_2O_2 concentration.

In order to understand the tangential component of the electric field we look at the transport of ions from anode to cathode. In the absence of significant bulk charge, as is evident in figure 2(b), current is carried predominantly in an Ohmic manner. Equating scaling of electromigration current and the cathodic current gives

$$E_{\text{tan}} \sim Da_a \quad (20)$$

In addition to governing transport of cations from anode to cathode, this component of the electric field will also affect the average zeta potential of the cathode. In other words, even if $Da_a = Da_c$ and thus $\phi_{\infty,0} = 0$, the fact that the potential at the anode outside of the double layer must be higher than the potential at the cathode to drive transport from one to the other means that ϕ_{∞} must be induced to equalize the average reaction rates. This contribution to the net potential will scale as the electric field multiplied by the length scale over which it acts.

We estimate the coefficients associated with this scaling and account for the quadratic dependence of the reaction rate on the H^+ concentration at the cathode by starting with the equation for bulk charge transport

$$\nabla \cdot (\sigma \mathbf{E}) = 0 \quad (21)$$

where $\sigma = D_+c_+ + D_-c_-$ the conductivity and \mathbf{E} the electric field. This equation, a formulation of Ohm's law, is asymptotically valid in the electroneutral bulk for small ϵ . We then, using a heuristic model based on Ramos' work [8] on Alternating Current Electro-Osmosis, assume that the outer electric field lines are semi-circular. This gives a bulk current of

$$\begin{aligned} i &= \sigma E & (22) \\ &= (D_+ + D_-) \frac{\phi_{\text{tan}}(-x) - \phi_{\text{tan}}(x)}{\pi x} & (23) \end{aligned}$$

where E is magnitude of the electric field along the field line starting at $-x$ just outside the electric double layer and ending at x and i the current density along it. We have also assumed $c_+ = c_- = 1$ outside the double layer. The value of E for each field line comes from the difference between the potential at the ends of the field line divided by its length. (23) is valid in the range $0 < x < 1/4$ where current lines travel from the anode to the right to the cathode without passing through the periodic boundary. We restrict our analysis to this region for simplicity and without loss of generality because the problem is symmetric about the center of each electrode. We will use (17) along with (23)

to predict an i which is constant along the surface. While this is not generally true at the cathode where i depends on c_+ and therefore is a function x , this model provides a useful approximation

$$\phi_{\text{tan}}(x) = \frac{-Da_a \pi x}{2(1 + D_-/D_+)} \quad (24)$$

Now that we have an estimate for the tangential variation of the electric potential, we can calculate an estimate of ϕ_∞ which accounts for it. Previously, to find $\phi_{\infty,0}$, we assumed that the potential drop across the double layer, and hence the surface concentration and reaction flux were independent of x . We now relax this assumption and include the combined potential difference across the double layer

$$\zeta(x) = \phi(x, y = 0) - \phi(x, 1 \gg y \gg \epsilon) \quad (25)$$

$$= -(\phi_\infty + \phi_{\text{tan}}) \quad (26)$$

This definition of ζ (25) comes from the local zeta potential representing the potential difference between the surface and a location far from the thin double layer based on inner scales $y \gg \epsilon$, but still close to the surface relative to outer scales $1 \gg y$. In other words, the potential difference between the surface and matching location between inner and outer solutions. The negative sign in (26) comes from our choice to reference potentials to the surface as given by the boundary condition of ϕ in (8) meaning that $\phi(x, y = 0) = 0$.

At steady-state, the surface reactions constitute the only species transport into or out of the domain. Setting the total flux at the cathode equal to that at the anode by integrating over the surface gives

$$\int_0^{1/4} j^+(x, y = 0) dx = - \int_{-1/4}^0 j^+(x, y = 0) dx \quad (27)$$

$$\int_0^{1/4} (e^{-\zeta})^2 D_+ Da_c dx = \frac{\lambda}{4} D_+ Da_a \quad (28)$$

where we have restricted our integral to be over the half of the cathode where (24) gives an estimate for the contribution of transport to the potential difference across the double layer. In (28) we have again assumed that the concentration of c_+ is uniform and equal to the reservoir concentration outside of the double layer and Boltzmann distributed within it. Because we have included only H^+ and OH^- in the model, the combination of bulk water equilibrium and electroneutrality will prevent bulk concentration gradients. However, when additional species are present, pH gradients will arise [14], and the variation in c_+ outside of the double layer will need to be accounted for. The domain is symmetric about the center of the anode and cathode, so the current through the other half of the cathode ($1/4 < x < 1/2$) will come from the other half of the anode ($-1/2 < x < -1/4$). Solving for

ϕ_∞ gives

$$\phi_\infty = \phi_{\infty,0} + \frac{1}{2} \ln \left(\frac{\beta Da_a}{1 - \exp(-\beta Da_a)} \right) \quad (29)$$

where $\beta = \pi/4(1 + D_-/D_+)$. In order to evaluate these models and scalings, we performed simulations over a broad range of anode and cathode Damköhler numbers. Figure 5 shows a comparison between ϕ_∞ from those simulations and the results of our model.

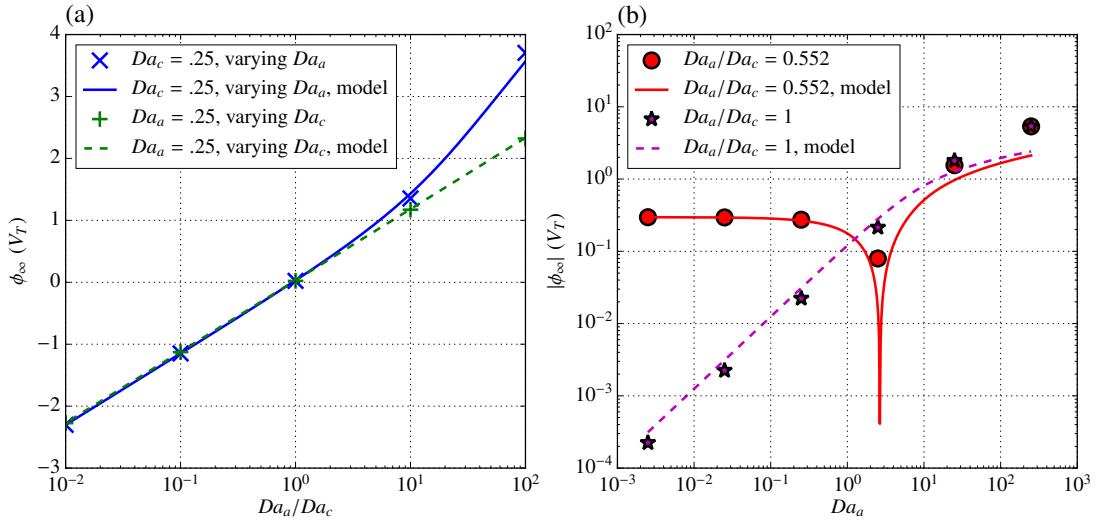


Figure 5: (Color online) Scaling of ϕ_∞ and comparison of simulation with model (29). (a) Scaling with Damköhler ratio showing the predicted logarithmic scaling when Da_a is small. (b) Scaling with Da_a for two fixed values of Da_a/Da_c .

In figure 5a cases where one of the Damköhler numbers is fixed and the other varied are shown, and very good agreement is observed over the entire range studied. Experimentally varying this ratio would be difficult because it depends on the ratio of reaction rate coefficients, however some variation may be possible by choosing different electrode materials. Figure 5b shows cases where the ratio of the Damköhler numbers is fixed and their magnitude is varied together representative of varying the concentration of H_2O_2 . Over most of the parameter space good agreement is observed except when Da_a becomes very large $O(100)$ and the model assumptions used to determine the component of ϕ_∞ caused by tangential transport break down. Additionally, at $Da_a = 2.5$ and a ratio of $Da_a/Da_c = .552$, some error is apparent because ϕ_∞ changes sign near this point making the result on the log-scale highly sensitive to the exact Damköhler number at which this sign change occurs and appear as a sharp feature. Both of these plots demonstrate that despite the many assumptions in the model, it is

able to accurately capture not merely the scaling, but the induced net potential in a broad parameter space.

To evaluate our predicted linear scaling of the tangential electric field with Da_a , figure 6 shows a comparison of our model

$$E_{\text{tan}} = -\frac{d\phi_{\text{tan}}}{dx} \quad (30)$$

$$= 2\beta Da_a \quad (31)$$

with E_{tan} from the simulations defined as $\max(E_x(x=0, y))$. We again see that the scaling is quite accurate over the entire range simulated with the predicted linear behavior when Da_a is varied and almost no change when Da_c is varied while Da_a is held constant. Additionally, our simple model is able to estimate the magnitude of the tangential electric field to within an $O(1)$ constant over the entire range.

Our model for the electric field (31) predicts that it should depend on the diffusivities of both species. In contrast, previous studies [17] found that it should depend only on the ionic strength and H^+ diffusivity. They argue that the conductivity shouldn't be important because only H^+ ions carry net current. However, when bulk water equilibrium reactions are accounted for, current in the bulk can be carried by OH^- ions which are generated by water splitting near the cathode and recombine with H^+ ions near the anode leading to a dependence of the electric field on their diffusivity.

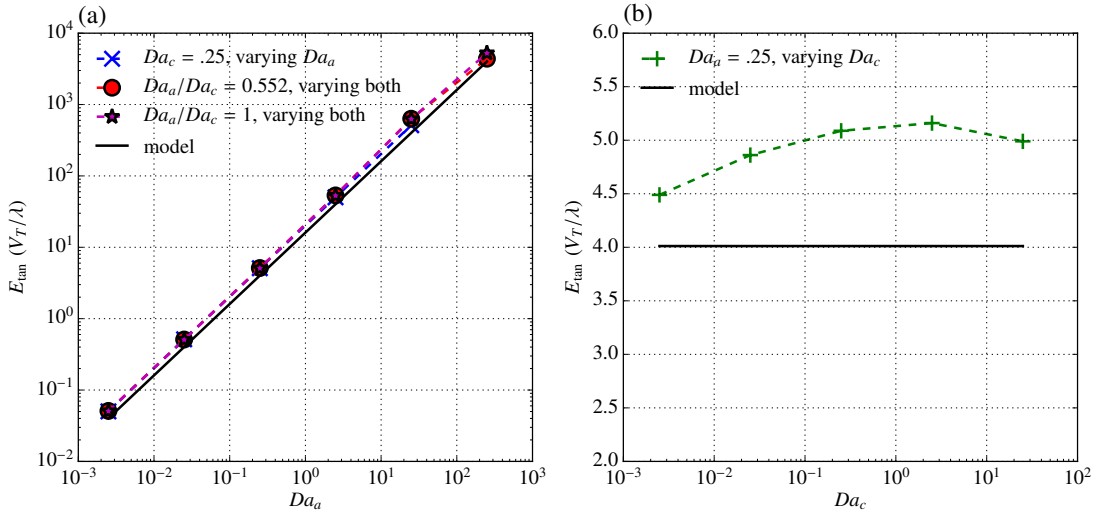


Figure 6: (Color online) Scaling of tangential electric field with Damköhler numbers. (a) shows that as predicted E_{tan} scales linearly with Da_a . (b) shows the independence of E_{tan} from Da_c .

The velocity of the flow induced by the micropump provides a useful measure of the ability of the reaction-induced convection to provide additional transport on top of diffusion. From a balance of the electric body force and diffusive terms in the momentum equations, the velocity should scale as the product of ζ and E_{tan} . For our model, we use the Helmholtz-Smoluchowski formula for electroosmotic flow past a flat charged surface, $u_{\text{slip}} = -\varepsilon E\zeta/\mu$ valid for slip associated with thin equilibrium double layers. Corrections for quasi- and non-equilibrium double layers, due to passage of current, also exist and could be included [51]. In our dimensionless formulation, this gives

$$u_{\text{slip}}(x) = -\kappa E_{\text{tan}}\zeta(x) \quad (32)$$

$$= \kappa\beta Da_a \left(\ln \frac{Da_a}{Da_c} + \ln \frac{\beta Da_a}{1 - \exp(-\beta Da_a)} - 2\beta Da_a x \right) \quad (33)$$

We evaluate this predicted slip velocity by comparing the predicted velocity at $x = 0$ with the slip velocity from our simulations $\max(u_x(x = 0, y))$ in figure 7. When $\phi_{\infty,0}$ is dominant, our model predicts that the velocity should be proportional to the quantity $Da_a \ln(Da_a/Da_c)$. From figure 7a we see that the velocity does indeed scale with this quantity and that our model predicts the maximum simulated velocity to within an $O(1)$ in all cases. In figure 7b a comparison is shown for the case where $Da_a/Da_c = 1$ and hence $\phi_{\infty,0} = 0$. Again for this case agreement to within an $O(1)$ constant is seen over many orders of magnitude change in the Damköhler number. Visually sharp features in figure 7a correspond to changes in the sign of the velocity, similar to those observed figure 5. We can also see from this figure that our earlier assumption that the nonlinear inertial term $\mathbf{u} \cdot \nabla \mathbf{u}/Sc$ is small relative to the other terms in the momentum is reasonable by comparing the inertial and viscous terms. The largest velocities here are $u \sim O(10^2)$, with the smallest length scale $l \sim \epsilon O(10^{-3})$. This means that the inertial term, which scales as $(1/Sc)u^2/l$, can be at most $O(10^4)$ while the viscous term, which scales as u/l^2 will be $O(10^8)$, a difference of four orders of magnitude.

4 Discussion and Conclusions

In this work we have modeled the reaction-induced electroconvection generated by the electrochemical decomposition of hydrogen peroxide on platinum and gold surfaces. Based on observations from our direct numerical simulations, we have developed a simple model without any tuning parameters which is able to predict both the induced electric potentials and flow velocity magnitudes to within a factor of ≈ 2 over a broad range of Damköhler numbers. This model can be used to aid in experimental design of systems using this reaction induced flow to provide additional near-surface mixing. It can also be modified to provide estimations for systems which involve other electrochemical reactions.

Although the developed model agrees well with simulations over the parameter space investigated, one important question which remains to be addressed in future studies is the effect of additional charged species on the system. Our model and simulations assume ideal water while in experimental

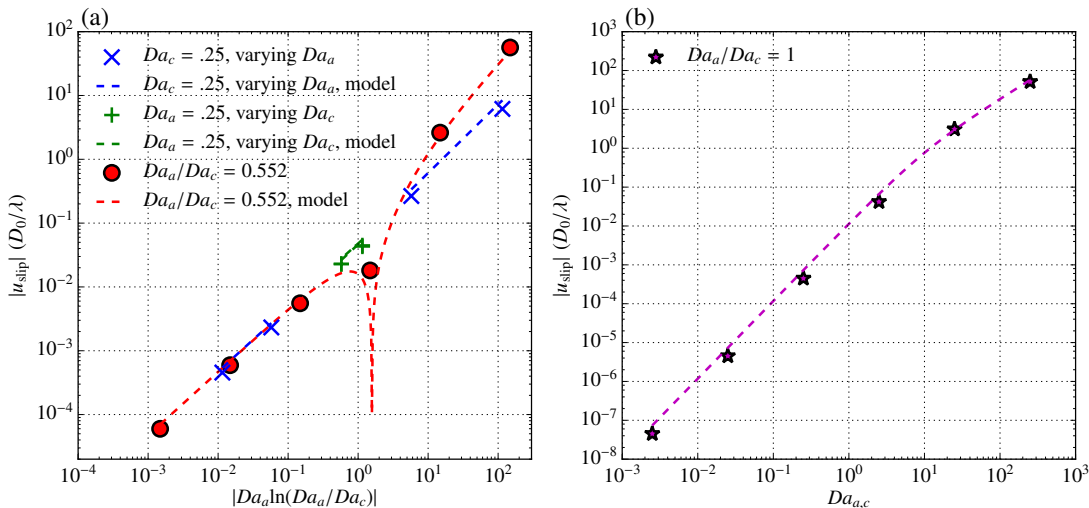


Figure 7: (Color online) Comparison of maximum tangential velocity predicted by our model (dashed lines) with simulations (symbols). (a) comparison for $Da_a/Da_c \neq 1$. (b) comparison for $Da_a/Da_c = 1$.

systems there will always be other ionic species due to either contaminants or their being added to induce other electrochemical reactions. The combination of the ideal water model and bulk electroneutrality mean that significant bulk pH and salt concentration gradients can not develop in our simulations and that double layers must remain in equilibrium.

5 Acknowledgements

Scott M. Davidson was supported by a Robert and Katherine Eustis Stanford Graduate Fellowship and by the National Science Foundation Graduate Research Fellowship under Grant No. DGE-114747. Ali Mani and Scott M. Davidson were supported by the National Science Foundation under Award #1553275. Rob G.H. Lammertink would like to acknowledge the Netherlands Organisation for Scientific Research (NWO, Vici project stirring the boundary layer).

References

- [1] Timothy R. Kline, Walter F. Paxton, Yang Wang, Darrell Velegol, Thomas E. Mallouk, and Ayusman Sen. Catalytic micropumps: Microscopic convective fluid flow and pattern formation. *Journal of the American Chemical Society*, 127(49):17150–17151, 2005.

- [2] Walter F. Paxton, Shakuntala Sundararajan, Thomas E. Mallouk, and Ayusman Sen. Chemical locomotion. *Angewandte Chemie International Edition*, 45(33):5420–5429, aug 2006.
- [3] Chao Zhou, Hua Zhang, Zeheng Li, and Wei Wang. Chemistry pumps: a review of chemically powered micropumps. *Lab Chip*, 16(10):1797–1811, 2016.
- [4] Todd M Squires, Robert J Messinger, and Scott R Manalis. Making it stick: convection, reaction and diffusion in surface-based biosensors. *Nature Biotechnology*, 26(4):417–426, apr 2008.
- [5] Martin Z. Bazant and Todd M. Squires. Induced-Charge Electrokinetic Phenomena: Theory and Microfluidic Applications. *Physical Review Letters*, 92(6):066101, feb 2004.
- [6] Todd M. Squires and Martin Z. Bazant. Induced-charge electro-osmosis. *Journal of Fluid Mechanics*, 509(1):217–252, 2004.
- [7] A. Ramos, H. Morgan, N. G. Green, and A. Castellanos. Ac electrokinetics: a review of forces in microelectrode structures. *Journal of Physics D: Applied Physics*, 31(18):2338, 1998.
- [8] Antonio Ramos, Hywel Morgan, Nicolas G Green, and Antonio Castellanos. AC Electric-Field-Induced Fluid Flow in Microelectrodes. *Journal of Colloid and Interface Science*, 217(2):420–422, sep 1999.
- [9] A. Ramos, A. González, A. Castellanos, N. G. Green, and H. Morgan. Pumping of liquids with ac voltages applied to asymmetric pairs of microelectrodes. *Physical Review E*, 67(5):056302, may 2003.
- [10] J L Anderson. Colloid Transport by Interfacial Forces. *Annual Review of Fluid Mechanics*, 21(1):61–99, jan 1989.
- [11] Timothy R. Kline, Jodi Iwata, Paul E. Lammert, Thomas E. Mallouk, Ayusman Sen, and Darrell Velegol. Catalytically driven colloidal patterning and transport. *Journal of Physical Chemistry B*, 110(48):24513–24521, 2006.
- [12] Walter F Paxton, Paul T Baker, Timothy R Kline, Yang Wang, Thomas E Mallouk, and Ayusman Sen. Catalytically induced electrokinetics for motors and micropumps. *Journal of the American Chemical Society*, 128(46):14881–8, nov 2006.
- [13] Michael E. Ibele, Yang Wang, Timothy R. Kline, Thomas E. Mallouk, and Ayusman Sen. Hydrazine fuels for bimetallic catalytic microfluidic pumping. *Journal of the American Chemical Society*, 129(25):7762–7763, 2007.

- [14] A. Afshar Farniya, M. J. Esplandiu, D. Reguera, and A. Bachtold. Imaging the proton concentration and mapping the spatial distribution of the electric field of catalytic micropumps. *Physical Review Letters*, 111(16):168301, oct 2013.
- [15] In Kook Jun and Henry Hess. A biomimetic, self-pumping membrane. *Advanced Materials*, 22(43):4823–4825, nov 2010.
- [16] Maria J. Esplandiu, Ali Afshar Farniya, and Adrian Bachtold. Silicon-Based Chemical Motors: An Efficient Pump for Triggering and Guiding Fluid Motion Using Visible Light. *ACS Nano*, 9(11):11234–11240, nov 2015.
- [17] Maria J. Esplandiu, Ali Afshar Farniya, and David Reguera. Key parameters controlling the performance of catalytic motors. *The Journal of Chemical Physics*, 144(12):124702, mar 2016.
- [18] J. L. Anderson, M. E. Lowell, and D. C. Prieve. Motion of a particle generated by chemical gradients Part 1. Non-electrolytes. *Journal of Fluid Mechanics*, 117(-1):107, apr 1982.
- [19] D. C. Prieve, J. L. Anderson, J. P. Ebel, and M. E. Lowell. Motion of a particle generated by chemical gradients. Part 2. Electrolytes. *Journal of Fluid Mechanics*, 148(-1):247, nov 1984.
- [20] Yiyang Hong, Misael Diaz, Ubaldo M. Córdova-Figueroa, and Ayusman Sen. Light-Driven Titanium-Dioxide-Based Reversible Microfireworks and Micromotor/Micropump Systems. *Advanced Functional Materials*, 20(10):1568–1576, may 2010.
- [21] Ran Niu, Patrick Kreissl, Aidan T. Brown, Georg Rempfer, Denis Botin, Christian Holm, Thomas Palberg, Joost de Graaf, and A. Sen. Microfluidic pumping by micromolar salt concentrations. *Soft Matter*, 13(7):1505–1518, 2017.
- [22] Peter Mitchell. Self-electrophoretic locomotion in microorganisms: Bacterial flagella as giant ionophores. *FEBS Letters*, 28(1):1–4, nov 1972.
- [23] P.E. Lammert, J. Prost, and R. Bruinsma. Ion Drive for Vesicles and Cells. *Journal of Theoretical Biology*, 178(4):387–391, feb 1996.
- [24] Sébastien Fournier-Bidoz, André C. Arsenault, Ian Manners, and Geoffrey A. Ozin. Synthetic self-propelled nanorotors. *Chemical communications (Cambridge, England)*, 424(4):441–443, 2005.
- [25] Walter F. Paxton, Ayusman Sen, and Thomas E. Mallouk. Motility of catalytic nanoparticles through self-generated forces. *Chemistry - A European Journal*, 11(22):6462–6470, nov 2005.
- [26] Philip M. Wheat, Nathan A. Marine, Jeffrey L. Moran, and Jonathan D. Posner. Rapid Fabrication of Bimetallic Spherical Motors. *Langmuir*, 26(16):13052–13055, aug 2010.

- [27] Yang Wang, Rose M. Hernandez, David J. Bartlett, Julia M. Bingham, Timothy R. Kline, Ayusman Sen, and Thomas E. Mallouk. Bipolar electrochemical mechanism for the propulsion of catalytic nanomotors in hydrogen peroxide solutions. *Langmuir*, 22(25):10451–10456, 2006.
- [28] Joseph Wang. Can Man-Made Nanomachines Compete with Nature Biomotors? *ACS Nano*, 3(1):4–9, jan 2009.
- [29] Jie Wu, Shankar Balasubramanian, Daniel Kagan, Kalayil Manian Manesh, Susana Campuzano, and Joseph Wang. Motion-based DNA detection using catalytic nanomotors. *Nature Communications*, 1(4):1–6, jul 2010.
- [30] Stephen J. Ebbens, Jonathan R. Howse, S. Balasubramanian, S. Sarrayasamitsathit, K. M. Manesh, G.-U. Flechsig, J. Wang, J. Wang, and V. H. Crespi. In pursuit of propulsion at the nanoscale. *Soft Matter*, 6(4):726, 2010.
- [31] Samudra Sengupta, Michael E. Ibele, and Ayusman Sen. Fantastic Voyage: Designing Self-Powered Nanorobots. *Angewandte Chemie International Edition*, 51(34):8434–8445, aug 2012.
- [32] Ramin Golestanian, Tanniemola B. Liverpool, and Armand Ajdari. Propulsion of a Molecular Machine by Asymmetric Distribution of Reaction Products. *Physical Review Letters*, 94(22):220801, jun 2005.
- [33] J. L. Moran, P. M. Wheat, and J. D. Posner. Locomotion of electrocatalytic nanomotors due to reaction induced charge autoelectrophoresis. *Physical Review E*, 81(6):065302, jun 2010.
- [34] Jeffrey L. Moran and Jonathan D. Posner. Electrokinetic locomotion due to reaction-induced charge auto-electrophoresis. *Journal of Fluid Mechanics*, 680:31–66, jun 2011.
- [35] Jeffrey L. Moran and Jonathan D. Posner. Role of solution conductivity in reaction induced charge auto-electrophoresis. *Physics of Fluids*, 26(4):042001, apr 2014.
- [36] E. Yariv. Electrokinetic self-propulsion by inhomogeneous surface kinetics. *Proceedings of the Royal Society A: Mathematical, Physical and Engineering Sciences*, 467(2130):1645–1664, jun 2011.
- [37] Benedikt Sabass and Udo Seifert. Nonlinear, electrocatalytic swimming in the presence of salt. *Journal of Chemical Physics*, 136(21):214507, jun 2012.
- [38] Amir Nourhani, Vincent H. Crespi, and Paul E. Lammert. Self-consistent nonlocal feedback theory for electrocatalytic swimmers with heterogeneous surface chemical kinetics. *Physical Review E*, 91(6):062303, jun 2015.

- [39] Patrick Kreissl, Christian Holm, and Joost De Graaf. The efficiency of self-phoretic propulsion mechanisms with surface reaction heterogeneity. *Journal of Chemical Physics*, 144(20):204902, may 2016.
- [40] Aidan T. Brown, Wilson C. K. Poon, Christian Holm, Joost de Graaf, Q. He, D. Velegol, R. Golestanian, S. J. Ebbens, and T. Mallouk. Ionic screening and dissociation are crucial for understanding chemical self-propulsion in polar solvents. *Soft Matter*, 13(6):1200–1222, 2017.
- [41] Simon B. Hall, Emad A. Khudaish, and Alan L. Hart. Electrochemical oxidation of hydrogen peroxide at platinum electrodes. Part 1. An adsorption-controlled mechanism. *Electrochimica Acta*, 43(5-6):579–588, 1998.
- [42] Simon B. Hall, Emad A. Khudaish, and Alan L. Hart. Electrochemical oxidation of hydrogen peroxide at platinum electrodes. Part II: effect of potential. *Electrochimica Acta*, 43(14-15):2015–2024, may 1998.
- [43] Jerome F.L Duval, Geertje K. Huijs, Wim F Threels, Johannes Lyklema, and Herman P. van Leeuwen. Faradaic depolarization in the electrokinetics of the metalelectrolyte solution interface. *Journal of Colloid and Interface Science*, 260(1):95–106, apr 2003.
- [44] Elif Karatay, Clara L. Druzgalski, and Ali Mani. Simulation of Chaotic Electrokinetic Transport: Performance of Commercial Software versus Custom-built Direct Numerical Simulation Codes. *Journal of Colloid and Interface Science*, 446:67–76, jan 2015.
- [45] Kambiz Salari and Patrick Knupp. Code verification by the method of manufactured solutions. Technical report, Sandia National Labs., Albuquerque, NM (US); Sandia National Labs., Livermore, CA (US), jun 2000.
- [46] C. L. Druzgalski, M. B. Andersen, and A. Mani. Direct numerical simulation of electroconvective instability and hydrodynamic chaos near an ion-selective surface. *Physics of Fluids*, 25(11):110804, nov 2013.
- [47] Clara Druzgalski and Ali Mani. Statistical analysis of electroconvection near an ion-selective membrane in the highly chaotic regime. *Physical Review Fluids*, 1(7):073601, nov 2016.
- [48] Scott M. Davidson, Mathias B. Andersen, and Ali Mani. Chaotic induced-charge electro-osmosis. *Physical Review Letters*, 112(12), mar 2014.
- [49] S.M. Davidson, M. Wessling, and A. Mani. On the Dynamical Regimes of Pattern-Accelerated Electroconvection. *Scientific Reports*, 6, 2016.

- [50] Martin Bazant, Katsuyo Thornton, and Armand Ajdari. Diffuse-charge dynamics in electrochemical systems. *Physical Review E*, 70(2), aug 2004.
- [51] I. Rubinstein and B. Zaltzman. Electro-osmotic slip of the second kind and instability in concentration polarization at electrodialysis membranes. *Mathematical Models and Methods in Applied Sciences*, 11(02):263–300, mar 2001.